Entrance-channel effects in quasifission reactions

B. B. Back, P. B. Fernandez, B. G. Glagola, D. Henderson, S. Kaufman, J. G. Keller,* S. J. Sanders,† F. Videbæk,‡ T. F. Wang,§ and B. D. Wilkins
Physics Division, Argonne National Laboratory, Argonne, Illinois 60439
(Received 25 October 1995)

The entrance-channel dependence of the distribution of reaction strength has been studied for three systems, namely $^{32}S+^{182}W$, $^{48}Ti+^{166}Er$, and $^{60}Ni+^{154}Sm$, which all lead to the compound system ^{214}Th in complete fusion reactions. The cross sections for elastic/quasielastic scattering, deeply inelastic, and fissionlike processes were measured at beam energies of $E_{lab}=166$, 177, 222, 260 MeV for $^{32}S+^{182}W$, $E_{lab}=220$, 240, 270, 298 MeV for $^{48}Ti+^{166}Er$, and $E_{lab}=339$, 390, 421 MeV for $^{60}Ni+^{154}Sm$, respectively. The maximum contribution of complete-fusion fission processes to the fissionlike cross section is estimated on the basis of expected angle-mass correlations for such reactions. The results show a strong entrance-channel dependence as predicted by the extra-push model.

PACS number(s): 25.70.Jj, 25.85.−w

I. INTRODUCTION

Quasifission processes have been experimentally identified as a substantial component of the total reaction cross section for low energy ($\leqslant 10$ MeV/u) heavy-ion induced collisions where the projectile mass exceeds 20 mass units [1–6]. Quasifission reactions are binary processes that exhibit some of the characteristics of fusion-fission events, such as a full relaxation of the relative kinetic energy and a considerable transfer of mass between the two fragments. The basic difference between fusion fission and quasifission is that compound nucleus formation is not achieved in the latter mechanism. Quasifission can be thought of as a bridge between deep-inelastic scattering, where the relative kinetic energy between the fragments can be fully damped, but the mass asymmetry of the entrance channel is mostly preserved, and compound nucleus fission reactions, where all memory of the entrance channel is lost.

One possible explanation for the occurrence of quasifission in reactions induced by heavy projectiles, $A_P \geqslant 20$, is that in these cases the angular momentum brought into the system is large enough to cause the disappearance of the fission barrier at large partial waves. Without a fission barrier, compound nucleus formation cannot take place. In this interpretation [7], the onset of quasifission is a static property of the completely fused system, independent of the formation process, as long as the angular momentum involved is large enough to make the fission barrier disappear. The relative importance of quasifission would then depend strongly on the bombarding energy, accounting for an increasingly larger fraction of the total reaction cross section as more angular momentum is brought into the reaction.

The extra-push model proposed by Swiatecki [8,9] provides another interpretation. It is based on dynamical trajectory calculations that include the effects of the potential energy surface, the mass tensor and one-body dissipation. The model shows that the quasifission processes occur in heavy systems for partial waves leading to a strong overlap of the two interacting ions in the entrance channel. This allows for rapid mass transfer and energy equilibration between the two ions that reseparate without having gone through a complete fusion stage [2–6]. The term quasifission arises from the fact that final distributions in mass and kinetic energy resemble those of normal compound fission. By virtue of describing the reaction dynamics in the entrance channel, this model predicts strong and well defined entrance channel dependences for the quasifission process.

To test these two interpretations of the quasifission process, we have measured the angular distribution of the reaction products for three different projectile-target combinations at several bombarding energies, all leading to the same compound nucleus ^{214}Th. We studied the distribution of the reaction strength and the characteristics of quasifission for the reactions $^{32}S+^{182}W$, $^{48}Ti+^{166}Er$, and $^{60}Ni+^{154}Sm$. The results for the $^{32}S+^{182}W$ reaction presented here have been published previously [10].

Section II describes the experimental setup. In Sec. III we describe the data analysis procedure, while Sec. IV deals with the discussion of our results.

II. EXPERIMENT

The experiments were carried out at Argonne National Laboratory, using beams from the superconducting linear accelerator ATLAS. Figure 1 shows a sketch of the experimental setup, while Table I lists the relevant parameters for the reactions studied. Only in the case of the ^{32}S induced reactions were fissionlike fragments detected at backward angles; the heavier projectiles imparted more forward momentum to the system, and the energy of the fissionlike fragments emitted in the backward direction in the laboratory frame was too low for detection. The reaction products were detected in 400 mm^2 silicon surface barrier detectors operated in singles mode, and positioned at distances of 40–70 cm from the target. An additional small area silicon detector was used to

*Now at GSI, D-6100 Darmstadt, Germany.
†Now at University of Kansas, Lawrence, Kansas 66045.
‡Now at Brookhaven National Laboratory, Upton, New York.
§Now at Lawrence Livermore National Laboratory, Livermore, California 94550.

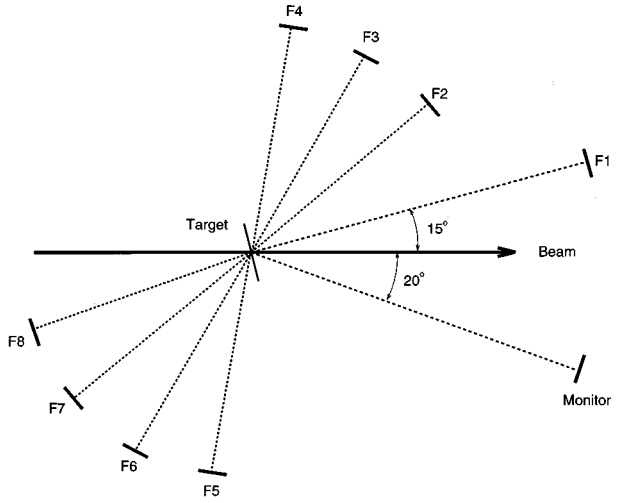

FIG. 1. Typical detector arrangement used in the present work.

monitor Rutherford scattering at forward angles for cross section normalization. The silicon detectors measured both the energy of the reaction products and their time of flight with respect to the time structure of the beam. The pulsed beam had a repetition rate of 12 MHz, or 82 ns between beam bursts. This time interval between bursts was adequate, since typical flight times for fission fragments ranged up to approximately 60 ns. The overall time resolution for the elastically scattered beam particles was of the order of 300 ps.

The energy calibration for the detectors was obtained from elastic scattering data at the different beam energies and by measuring α particles and fission fragments emitted from a ^{252}Cf source. Detector solid angles were calculated from the aperture area and distance from the target although the relative solid angle between the detectors was determined with higher precision by counting α particles from a ^{252}Cf source placed at the target position. The time dispersions were measured using a pulser triggered by a signal derived from the linac radio frequency. The offset of the time calibration was computed at each beam energy from the measured position of the elastic scattering peak in the time spectrum and the known flight time from the target to the detector.

III. DATA ANALYSIS

The analysis of the data was carried out by reconstructing the primary reaction kinematics event by event. The mass and kinetic energy of the primary fragments in the center-of-mass system were determined for each event assuming a binary reaction channel. This assumption is well justified by the systematics for fission fragment folding angle distributions, which show that incomplete momentum transfer reactions are strongly suppressed at beam energies below 10 MeV/u [11]. Furthermore, since the targets used in this experiment, ^{154}Sm, ^{166}Er, and ^{182}W all have very high fission barriers, sequential fission following transfer and inelastic scattering reactions is strongly suppressed and is not expected to contribute to the observed fission yield.

TABLE I. Reaction parameters.

Projectile	Target	Beam energy (MeV)	Target thickness [a] (μg/cm^2)	$\theta_{\rm lab}$ (deg)
^{32}S	^{182}W	166,177,222,260	100	10–170
^{48}Ti	^{166}Er	220,240,270,298	60	10–95
^{60}Ni	^{154}Sm	339,390,421	180	10–90

[a]All targets were evaporated on a thin ($\sim$20 μg/cm^2) carbon foil.

Several corrections to the measured energy and time-of-flight of the fissionlike fragments were made in order to carry out this reconstruction. The observed energy and time signals were corrected for the pulse-height defect and plasma delay associated with the measurement of heavy ions in silicon detectors. The pulse-height defect causes a reduction of the observed energy relative to the true energy, and the plasma delay refers to the delay of the timing signal with respect to the time of arrival of the ion in the detector. These effects are caused by the creation of a high-conductivity plasma along the trajectory of the heavy ion in the detector, which allows for the recombination of electron-hole pairs (thus decreasing the amplitude of the energy signal), and retards the charge collection process (thereby slowing down the timing signal) [12]. We have corrected for pulse height defect following the empirical formula of Ogihara *et al.* [13], who studied the systematics of the pulse height defect phenomenon in silicon detectors for a variety of ions ranging from ^{12}C to ^{127}I.

The plasma delay correction was assumed to depend linearly on the fragment mass; the constants for the plasma delay correction were determined from the measured time signals for the elastically scattered projectile ions and the corresponding recoils by comparing them to the expected flight times. The pulse height defect was typically of the order 8 MeV for symmetric fragments ($A=107$) at 160 MeV, while the plasma delay was less than 1.5 ns (the typical flight times for fission fragments were $\approx$50 ns).

We also corrected the measured fragment energy for losses in the target material, target backing, and the front gold electrode of the detectors, as well as for post-fission neutron evaporation, usually 2–5 mass units (depending on the bombarding energy). We estimate that the combined uncertainty from these corrections translates into a 3–4 mass units uncertainty in the fragment mass.

A typical two dimensional spectrum of the total kinetic energy (TKE) vs fragment mass obtained with this analysis is shown in Fig. 2. The TKE is defined as the total center-of-mass kinetic energy of both fissionlike fragments. The different components of the reaction cross section are readily identified: elastic/quasielastic scattering, deep-inelastic scattering, and fissionlike processes (fissionlike includes both fusion fission and quasifission). The fissionlike fragments follow the behavior expected from the Viola systematics [14], i.e., the total kinetic energy is given by the Coulomb repulsion between the two deformed fragments at the scission point. In the following, we discuss the individual components of the reaction cross sections, namely elastic/quasielastic scattering, deeply inelastic scattering and fissionlike processes.

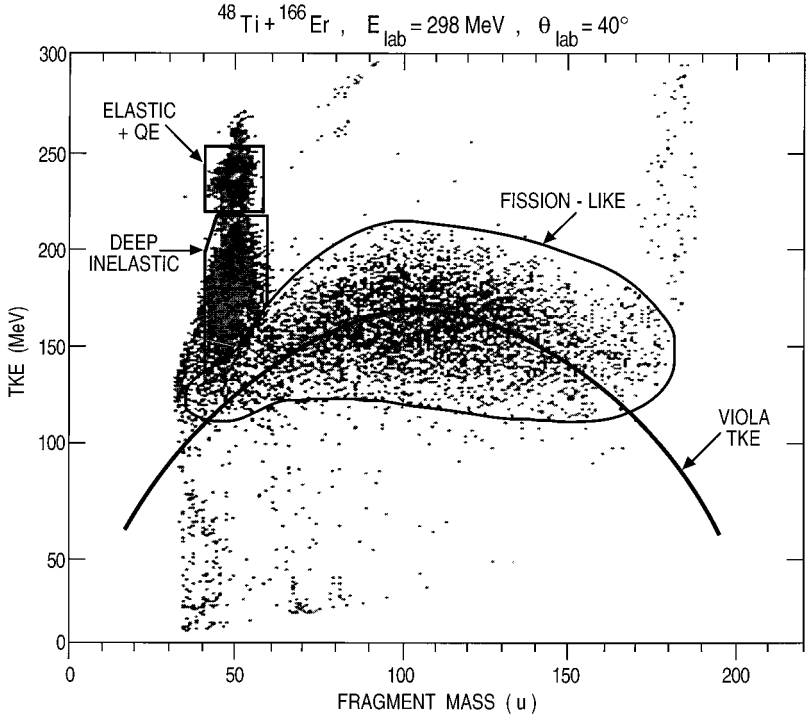

FIG. 2. Two-dimensional spectrum of the total kinetic energy, TKE, in the center-of-mass system plotted vs the mass of one of the fission fragments for the reaction ^{48}Ti+^{166}Er at $E_{lab}=298$ MeV and $\theta_{lab}=40°$. The regions corresponding to different reaction groups are indicated.

IV. RESULTS AND DISCUSSION

Angular distributions for the individual components of the reaction cross section are obtained by applying the appropriate laboratory to center-of-mass Jacobian and normalization factors to the two-dimensional spectra of total kinetic energy TKE vs fragment mass spectra. We thus determined the center-of-mass angular distributions and angle-integrated cross sections for the elastic+quasielastic, deep-inelastic, and fissionlike processes.

A. Elastic/quasielastic scattering

In the present analysis, we include all processes with an energy dissipation of up to 8–15 MeV ($\approx$6% of the elastically scattered projectile energy) into the elastic/quasielastic yields, since the energy resolution is insufficient to distinguish between elastic scattering, inelastic excitations, and transfer processes. An example of the window used for computing the cross section is shown in Fig. 2. The resulting ratio of elastic/quasielastic cross sections to the Rutherford cross section for each of the entrance channels studied is shown in Fig. 3. The data exhibit the expected behavior, i.e., the ratio remains constant up to the grazing angle, beyond which it decreases exponentially as the interaction strength is removed from the elastic channel into the deep-inelastic and fissionlike processes. We note that the grazing angle moves forward with increasing bombarding energy; at the lowest energies, the grazing angle is so far back that deviations from Rutherford scattering could only be seen in the case of ^{32}S+^{182}W, where detectors covered the full angular range up to $\theta_{lab}=170°$.

We used the sum of differences method [15] to determine the total cross section for damped reactions, σ_{reac}, from the elastic/quasielastic angular distributions. According to this method the damped reaction cross section σ_{reac} is given by

$$\sigma_{reac}=2\pi\int_{\theta_{gr}}^{\pi}\sigma_{Ruth}\left(1-\frac{\sigma_{el}(\theta)+\sigma_{qe}(\theta)}{\sigma_{Ruth}}\right)\sin\theta\, d\theta. \quad (1)$$

The resulting values of σ_{reac} are listed in Table II. We observe a good agreement between this estimate of σ_{reac} and the sum of the deep-inelastic and fissionlike reaction cross sections determined directly from the data. This shows that the reaction channels measured in the present experiment exhaust the full reaction cross section.

B. Deep-inelastic scattering

The deep-inelastic events are identified as those with greater energy dissipation than the elastic/quasielastic components, namely energy losses larger than 8–15 MeV, and masses within $\approx$20% of the projectile mass (e.g., $\pm$10 mass units in the case of ^{48}Ti+^{166}Er). A representative deep-inelastic window used in the analysis is indicated in Fig. 2. The angular distribution of deep-inelastic products is obtained by integrating over fragment mass and total kinetic energy using the appropriate Jacobian in the transformation from the laboratory to the center-of-mass frame of reference. The results are displayed in Fig. 4. The solid curves through the data were used to compute the angle-integrated cross section; the dashed curves represent an attempt at estimating the error in the cross section. Comparing Fig. 4 and Fig. 3, we see that the deep-inelastic cross section peaks near the grazing angle θ_{gr}, as has been previously observed [10]. The deep-inelastic contribution could not be separated from the slit scattered beam at the most forward angles. However, it is believed that the main component of the deep-inelastic cross section is covered by the measurement.

The angle-integrated cross sections for deep-inelastic scattering, $\sigma_{D.I.}$, are listed in Table II. The errors in $\sigma_{D.I.}$ include an estimate of the uncertainty in the extrapolation of

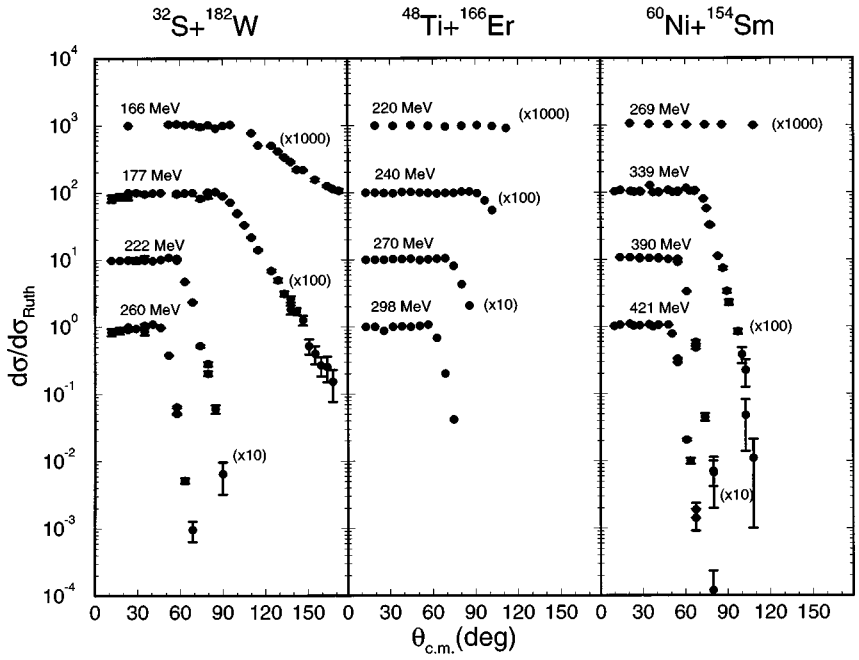

FIG. 3. Angular distributions for elastic/quasielastic scattering normalized to the Rutherford cross section are shown for the three reactions studied.

the cross section to the forward angles. We observe that the deep inelastic process constitutes a substantial fraction of the reaction cross section in all the reactions studied here, even at the lowest beam energies near the barrier.

C. Fissionlike processes

The fissionlike processes are characterized by total kinetic energies which are well described by the Coulomb repulsion between the fragments at the scission point (see Fig. 2). For the ^{32}S+^{182}W and ^{48}Ti+^{166}Er reactions the fissionlike processes are clearly separated from the deep-inelastic processes centered at the masses of the target/projectile combination. However, for the ^{60}Ni+^{154}Sm system this separation is less pronounced, which contributes to the error on the cross section estimates in this case.

1. Angular distributions

The angular distribution $d\sigma/d\Omega$ of fissionlike fragments for the ^{32}S+^{182}W channel is shown in Fig. 5. The standard formalism for angular distributions of compound nucleus fission is given by [16]

$$W(\theta_{\text{c.m.}}) = \sum_{I=0}^{\infty} (2I+1)P(I) \sum_{K=-I}^{I} \frac{1}{2}(2I+1)\rho(K,I) \times |d^{I}_{0,K}(\theta_{\text{c.m.}})|^2. \quad (2)$$

Here, I is the spin of the fissioning system, K is the projection of the spin on the symmetry axis, $d^{I}_{0,K}(\theta_{\text{c.m.}})$ is the symmetric top wave function, $P(I)$ is the partial wave distribution as given by the extra-push model [6], and $\rho(K,I)$ is the saddle point K distribution assumed to be a Gaussian with

TABLE II. Angle-integrated cross sections.

Reaction	E_{lab} (MeV)	σ_{reac} (mb)	$\sigma_{\text{D.I.}}+\sigma_{\text{fis}}$ (mb)	$\sigma_{\text{D.I.}}$ (mb)	σ_{fis} (mb)	$\sigma_{\text{C.F.,max}}$ (mb)
^{32}S+^{182}W	166	365±30	355±65	175±65	180±20	<25
	177	680±50	630±70	210±55	420±45	<270
	222	1550±100	1375±125	430±75	945±100	<375
	260	1970±100	1830±220	605±160	1225±150	<545
^{48}Ti+^{166}Er	220		80±16		80±16	<50
	240	675±175	685±125	310±100	375±75	<150
	270	1170±100	1210±205	500±150	710±140	<265
	298	1620±60	1675±270	750±200	925±180	<345
^{60}Ni+^{154}Sm	339	1345±150	1295±190	395±60	900±180	<205
	390	1880±150	1790±260	530±65	1260±250	<195
	421	2100±150	1980±310	620±160	1360±270	<310

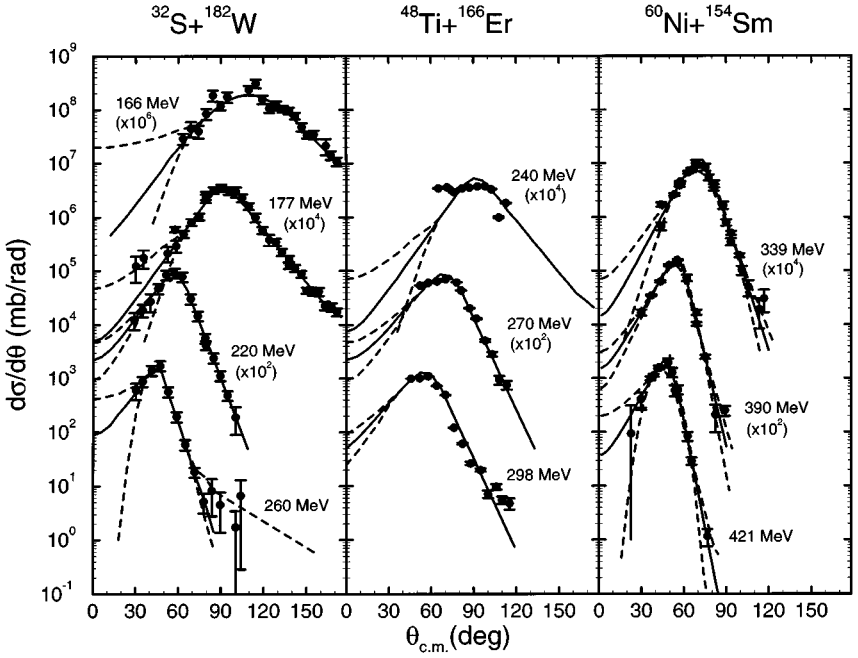

FIG. 4. Angular distributions for deep-inelastic scattering are shown. The solid curves represent fits to the data on the basis of which the angle-integrated cross sections are estimated. The uncertainties are based on the dashed curves.

variance K_0^2. The solid curves in Fig. 5 are fits to the data using Eq. (2). The two parameters that are varied in the fit are the overall normalization and the variance of the K distribution, K_0^2, which is related to the angular anisotropy in the angular distribution, $W(180°)/W(90°)$, through the approximate expression

$$\frac{W(180°)}{W(90°)} \approx 1 + \frac{\langle I^2 \rangle}{4K_0^2}. \tag{3}$$

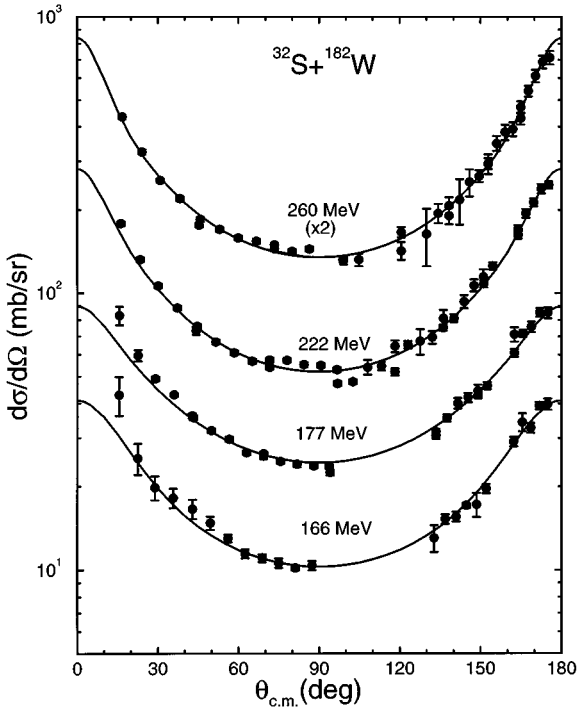

FIG. 5. Angular distributions for fissionlike fragments for the reaction ^{32}S+^{182}W. Solid curves represent the best fit to the data obtained by varying the K_0 parameter.

Since the angular distribution data extend to backward angles it was possible to make an accurate determination of the anisotropy, $W(180°)/W(90°)$, and, consequently, of K_0^2. Figure 6 shows K_0^2 as a function of the mean square angular momentum for the ^{32}S+^{182}W reaction. Also shown are the predictions for K_0^2 given by the saddle point model [16] using moments of inertia obtained from the finite range liquid drop model [18] (solid curve), and the scission point model [19] (dash-dotted curve). The measured values of K_0^2 are smaller than the saddle point predictions, indicating the presence of a larger than expected anisotropy, which is one of the possible signatures of a quasifission component. Since the experimental values lie between the saddle and scission point predictions, another possible interpretation is that the K_0^2 distribution is frozen sometime during the evolution of the system from the saddle point to the scission point. This alternative has been discussed in Ref. [3], where it was concluded that the deviations in the angular distribution are due to the failure to achieve complete fusion, and not to a deficiency of the saddle point model.

For the ^{48}Ti and ^{60}Ni induced reactions, we show the angular distribution for fission fragments for individual mass bins in Figs. 7 and 8. The solid curves are fits to the experimental data using Eq. (2) folded with an exponential decay function to reproduce the evident forward-backward asymmetry present in the data, i.e.,

$$\frac{d\sigma}{d\theta_{\text{c.m.}}} = 2\pi \sin\theta_{\text{c.m.}} e^{\beta(\theta_{\text{c.m.}} - \pi/2)} W(\theta_{\text{c.m.}}). \tag{4}$$

In these calculations the overall normalization and the angular slope parameter, β, were varied to reproduce the angular distributions. The variance of the K distribution, K_0^2, was fixed to the average of the values that produced the best fits for the mass bins near and at symmetry. We note that the mass bin $A = 106$–110 corresponding to the symmetric mass split is forward-backward symmetric as expected for binary

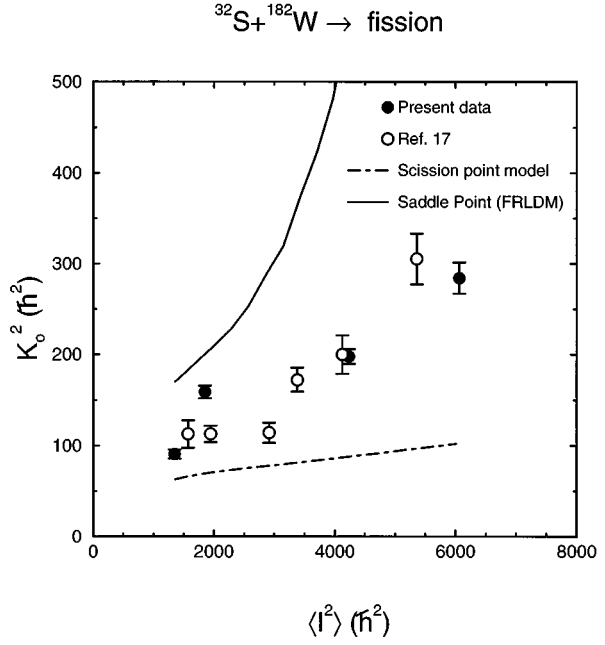

FIG. 6. Experimental values of K_0^2 for ^{32}S+^{182}W (solid points: present data; open points: Ref. [17]) are compared to the predictions of the saddle point model (solid curve) and the scission point model (dot-dashed curve).

reactions in all cases. For lighter fragment masses we find a large angular asymmetry, with the light fragments being preferentially emitted in the forward direction. This behavior is inconsistent with the binary decay of a completely fused system, and it is an indication that the reaction time is shorter or comparable to the rotational period of the interaction complex.

The above expression does not derive from any theoretical model of quasifission reactions, but is designed to account for the observed exponential behavior of $d\sigma/d\theta_{\mathrm{c.m.}}$. Assuming that the quasifission reactions correspond to partial waves smaller than those for the deep-inelastic scattering reactions and having longer interaction times, one would expect that the angular distribution of quasifission fragments, $|d\sigma/d\theta_{\mathrm{c.m.}}|_A$, in the mass range near the projectile would peak at an angle slightly forward of the maximum of the deep-inelastic angular distribution (indicated by the arrows in Fig. 8 for the ^{60}Ni+^{154}Sm reaction). The angular distributions for the mass bin $A=56-60$ do not show any indication of such a peak, however, but continue to rise exponentially toward smaller angles as do the distributions for other mass bins. In fact, the angle of maximum cross section, $d\sigma/d\theta_{\mathrm{c.m.}}$, appears to lie within the range $\theta=0°-20°$.

Figures 7 and 8 show that the angular asymmetry develops and increases with mass asymmetry. This trend is more directly displayed in Fig. 9, where the slopes, expressed in terms of the parameter β, are shown for the ^{48}Ti and ^{60}Ni induced reactions. The slopes are seen to develop gradually with mass asymmetry for both reactions, albeit at a higher rate for the ^{60}Ni+^{154}Sm reaction than for ^{48}Ti+^{166}Er. The curve for 339 MeV ^{60}Ni+^{154}Sm shows a small kink in the region of the projectile mass $A=60$ possibly indicating a contamination from deep-inelastic scattering events.

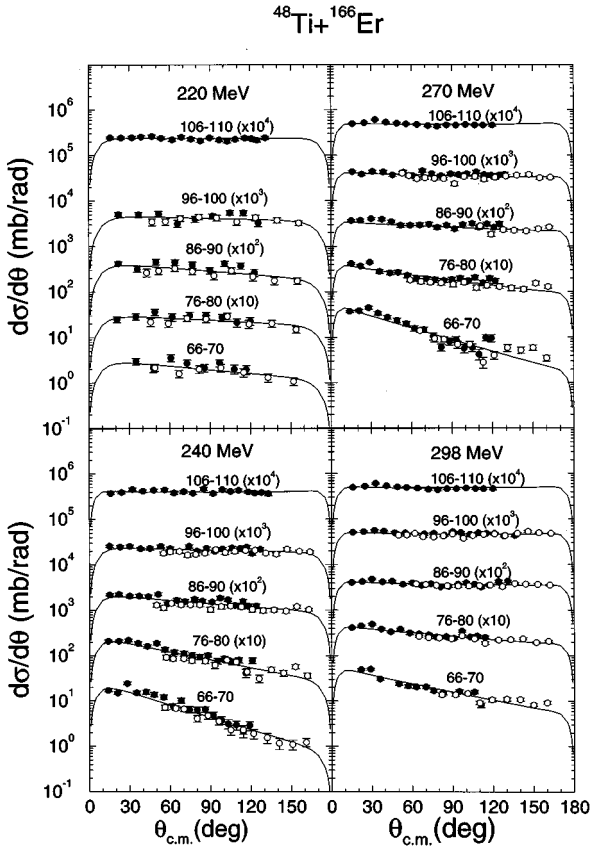

FIG. 7. Differential cross sections for fissionlike fragments for the ^{48}Ti+^{166}Er reaction for different fragment mass bins. The solid points correspond to the mass bin A, as indicated, whereas the open points belong to the mass bin $A_{\mathrm{C.N.}}-A$ plotted at $\pi-\theta_{\mathrm{c.m.}}$ reflecting the kinematic symmetry for two-body kinematics. The solid lines are best fits to the data using Eq. (4).

2. Cross sections

The total cross sections for fissionlike processes were obtained by integrating the differential cross sections for each bombarding energy. The resulting excitation functions for the angle-integrated cross sections are shown in Fig. 10 as solid circles and listed in Table II. The figure also shows the cross sections for damped reactions, $\sigma_{\mathrm{D.I.}}+\sigma_{\mathrm{fis}}$, the sum of the measured deep-inelastic and fissionlike cross sections as filled squares, and the estimate of the maximum fusion-fission contribution, $\sigma_{\mathrm{C.F.,max}}$, the determination of which will be discussed in detail in Sec. IV D. The sum of deep-inelastic and fissionlike cross sections exhausts, within errors, the total cross section for damped reactions derived from the elastic/quasielastic angular distributions; see Table II.

The solid curves in Fig. 10 result from an extra-push model calculation using the parameters obtained by Shen *et al.* [5,6]; σ_{touch} is the cross section for overcoming the interaction barrier, and it includes deep-inelastic, quasifission, and fusion-fission processes; σ_{cap} is the cross section for capture behind the conditional saddle point, i.e., quasifission and compound nucleus fission. In this model, the collision dynamics are considered explicitly along the whole reaction path. The model is very successful in describing the capture cross section for the ^{32}S and ^{48}Ti induced reactions,

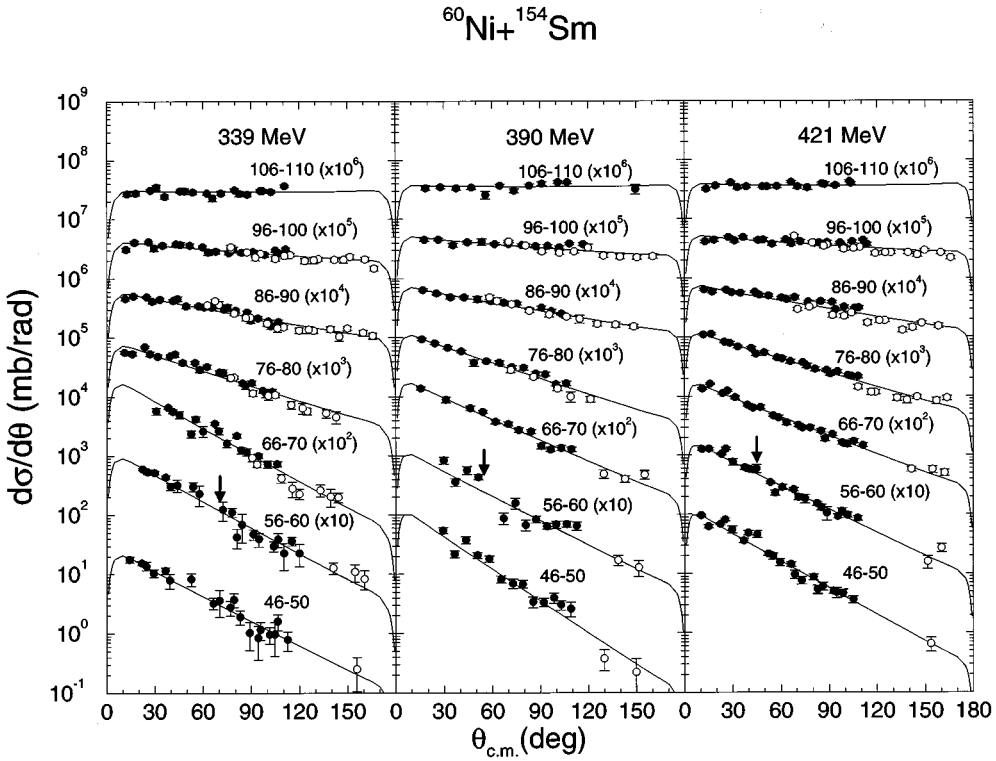

FIG. 8. Same as Fig. 7, but for the ^{60}Ni+^{154}Sm reaction.

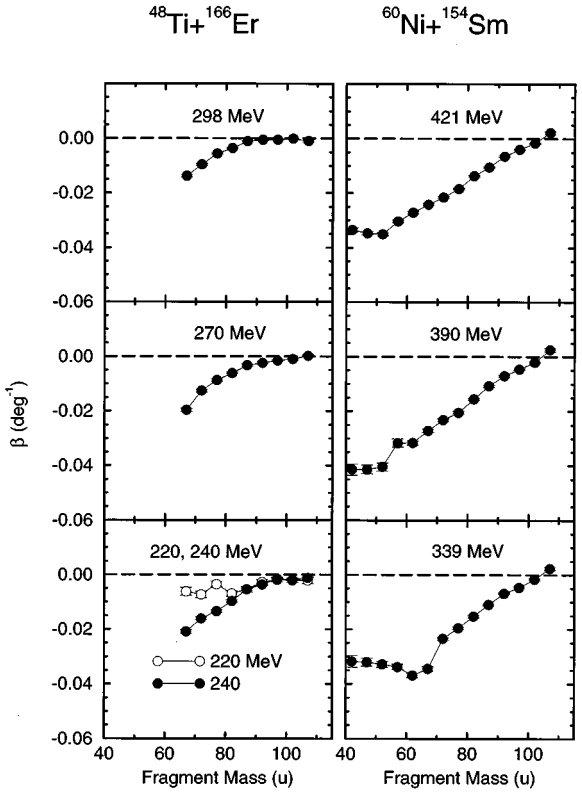

FIG. 9. The extracted value of the slope parameter, β [Eq. (4)] is plotted as a function of the fragment mass for ^{48}Ti+^{166}Er (left panels) and ^{60}Ni+^{154}Sm (right panels).

while it underpredicts the measured ^{60}Ni+^{154}Sm capture cross section. This discrepancy may be caused by the unavoidable inclusion of some deep-inelastic contribution in the analysis of the fissionlike data. The model is less successful in accounting for the deep-inelastic cross section, $\sigma_{\text{touch}}-\sigma_{\text{cap}}$. The calculation underpredicts the data, possibly due to the model assumption that deep-inelastic scattering processes are associated only with trajectories which proceed inside the interaction barrier.

3. Mass distributions

The mass distributions for the fissionlike fragments for the ^{48}Ti+^{166}Er and ^{60}Ni+^{154}Sm reactions were extracted by integrating the angular distribution for each mass bin and are shown in Fig. 11. The solid dots were derived from the total fissionlike cross section, while the open circles correspond to the maximum forward-backward symmetric angular distribution (obtained from the fit to the $A=107$ mass bin) commensurate with the data points at backward angles. The solid curves are discussed in Sec. IV D 3.

The standard deviations of the mass distributions for total fissionlike fragments, σ_A, are shown in Fig. 12 as a function of the excitation energy at the scission point, E^+, which is calculated as follows:

$$E^+ = E_{\text{exc}} + Q_{\text{sym}} - E_K - E_{\text{def}} - E_{\text{rot}}. \tag{5}$$

Here E_{exc} is the excitation energy of the compound system, Q_{sym} is the Q value for symmetric fission, E_K is the total kinetic energy estimated from the Viola systematics [14], E_{def} accounts for the fragment deformation energy (taken to be 12 MeV), and E_{rot} is the rotational energy at scission.

The solid line in Fig. 12 is the expected dependence of the width of the mass distribution on the excitation energy at the scission point, as derived from the statistical model treatment

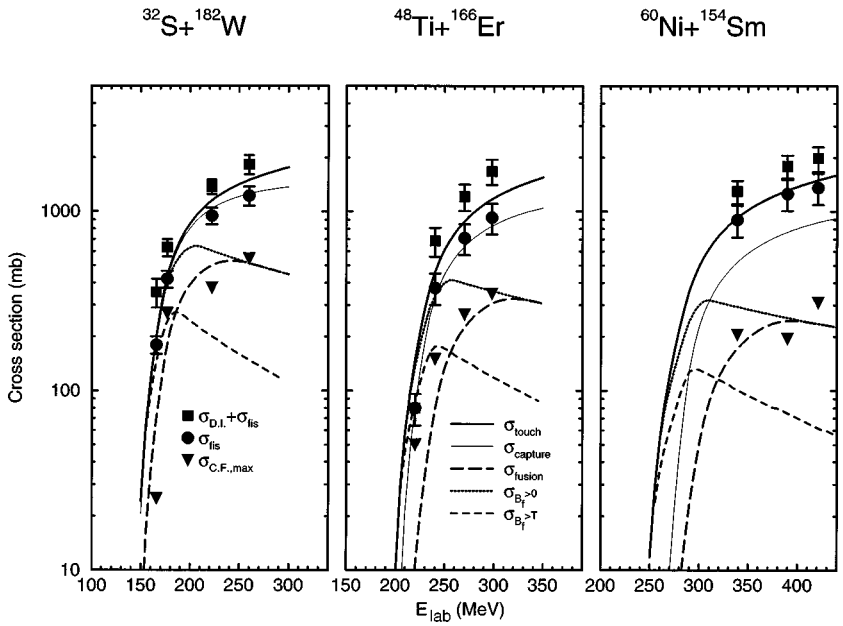

FIG. 10. Experimental cross sections for damped reactions, $\sigma_{\mathrm{D.I.}}+\sigma_{\mathrm{fis}}$ (solid squares), fissionlike processes, σ_{fis} (solid circles), and upper limits for complete fusion, $\sigma_{\mathrm{C.F.,max}}$ (solid triangles) are compared to extra push model predictions σ_{touch} (thick solid curve), $\sigma_{\mathrm{capture}}$ (thin solid curve), and σ_{fusion} (long-dashed curve). Limits for fusion based on the criteria $B_f>0$ and $B_f>T$ are shown as dotted and short dashed curves, respectively.

of the mass asymmetry degree of freedom, and consistent with the fusion-fission mechanism. Here it is assumed that the mass asymmetry potential can be approximated by a parabolic shape

$$U(A)=\frac{1}{2}k(A-A_S)^2, \tag{6}$$

where A is the fragment mass, A_S is the mass for symmetric fragmentation ($A_S=107$ for ^{214}Th), and k is a stiffness parameter for the mass asymmetry degree of freedom. A statistical model treatment leads to a variance of the fragment mass distribution given by

$$\sigma_A^2=\frac{T}{k}=\frac{1}{k}\sqrt{\frac{8.5E^+}{A}}, \tag{7}$$

where T is the scission point temperature and A is the mass of the system. The value of the stiffness parameter, $k=0.0048$ MeV/u^2 is determined from mass distributions for the reactions ^{12}C, ^{16}O+^{206}Pb [20] leading to compound nuclei of ^{218}Ra and ^{222}Th. These are close to the ^{214}Th system under study, but less likely to be contaminated by quasifission reactions and suffer from possible effects of high angular momenta.

Figure 12 illustrates that the mass widths for the ^{32}S+^{182}W and ^{48}Ti+^{166}Er reactions are essentially in agreement with the statistical model expectation although some deviations occur for the lower points for the ^{48}Ti+^{166}Er system. However, the data for the ^{60}Ni+^{154}Sm reaction displays a strong deviation from this model indicating the presence of a strong quasifission component.

In order to explore the possible effects of angular momentum on the observed mass widths, we have in Fig. 13 plotted the parameter $\sigma_A/(E^+)^{1/4}$ as a function of the mean square angular momentum $\langle I^2\rangle$ associated with the fissionlike cross section in order to remove the temperature effects. The mean square spin for which the fission barrier is expected to disappear, $(I_{B_f=0})^2$ [18], is indicated by an arrow. Note that at this point, 50% of the cross section corresponds to angular momenta for which the fission barrier has vanished, in a sharp cutoff approximation. Data points above this limit therefore must have a quasifission contribution of at least 50%. The fact that the reduced mass widths, $\sigma_A/(E^+)^{1/4}$,

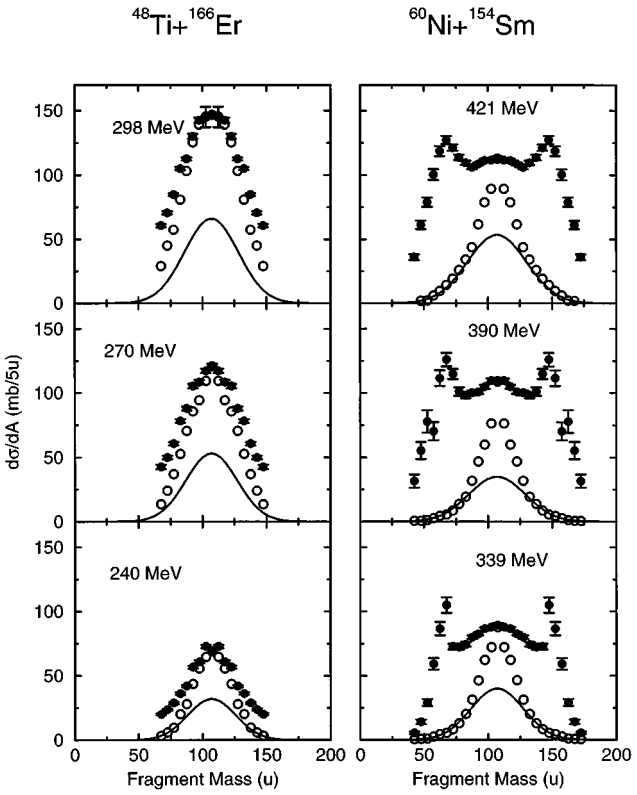

FIG. 11. Mass distributions for fissionlike fragments are shown as solid points for the ^{48}Ti+^{166}Er (left panels) and ^{60}Ni+^{154}Sm (right panels) systems. Open points represent upper limits imposed by requiring only forward-backward symmetry for each mass bin, whereas the solid curves represent upper limits for complete fusion; see text.

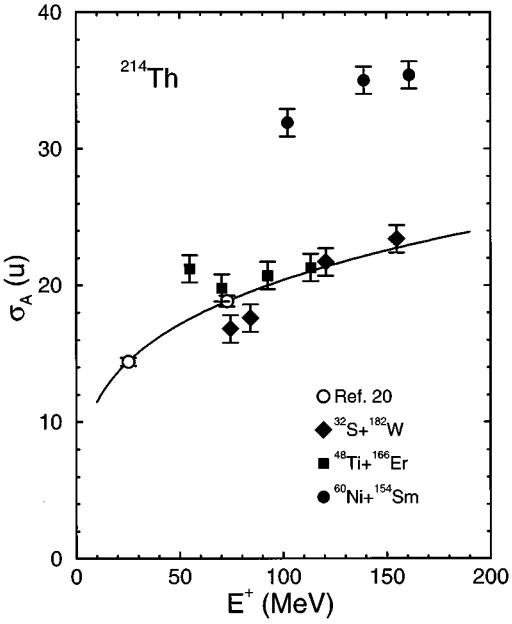

FIG. 12. The standard deviation of the mass distribution for fissionlike fragments is shown (solid points) as a function of excitation energy at the scission point, E^+, and compared to the scission point model estimate [solid curve, Eq. (7)], normalized to data with ^{12}C and ^{16}O beams [20] (open circles).

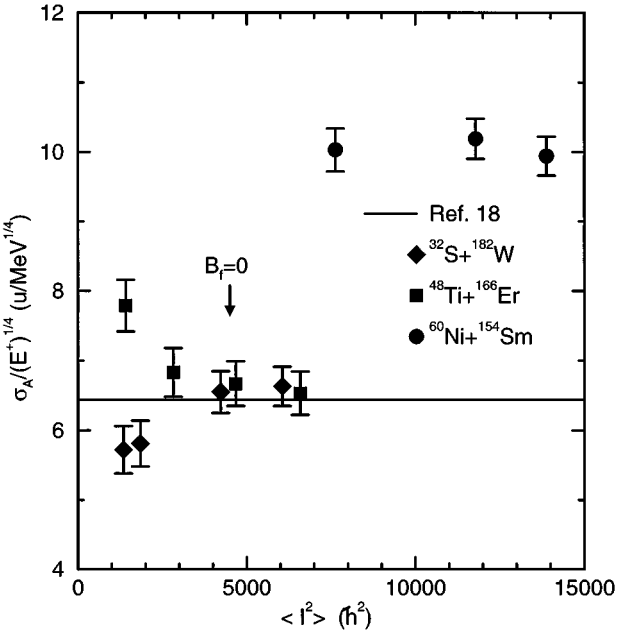

FIG. 13. The standard deviation of the mass distributions for fissionlike fragments (solid symbols) are plotted as a function of the mean square angular momentum, $\langle I^2 \rangle$, and compared to scission point model prediction (solid line).

follow the expectation based on a statistical equilibrium at the scission point even well above this point for the ^{32}S+ ^{182}W and ^{48}Ti+ ^{166}Er systems shows that this parameter by itself is not necessarily a reliable indicator for the onset of quasifission reactions [7]. The mass widths for the ^{60}Ni+ ^{154}Sm system, however, are substantially larger than expected on the basis of this model, although the mean square spin at the lowest beam energy is similar to those of the highest energy points for the ^{32}S+ ^{182}W and ^{48}Ti+ ^{166}Er systems. This effect is therefore associated with the more symmetric entrance channel and it is in qualitative agreement with the expectations of the extra push model [8].

In a quasifission process, the projectile-target system separates before the mass asymmetry degree of freedom has been fully equilibrated, and we therefore expect deviations from the above deduced expression for the width of the mass distribution. In the case of the asymmetric channels that we used to reach ^{214}Th, a possible signature for quasifission would be a larger σ_A^2 compared to the compound nucleus prediction [7].

D. Upper limits for complete fusion cross sections

In our study of entrance-channel effects on quasifission, we focus on three different signatures of this process: angular anisotropies that are larger than predicted by the liquid-drop model; broken fragment mass symmetry between forward-backward directions in the center of mass; and an increase in the width of the fragment mass distribution compared to the widths expected for fusion-fission. In this section we attempt to estimate the largest fraction of the observed fissionlike cross section which may arise from complete fusion, by requiring that each of these observables fulfill the expectations for fission of an equilibrated compound nucleus.

1. Forward-backward asymmetry

In compound nucleus fission, there is no preferential direction for the emission of fission fragments in the center of mass system, except for the anisotropy introduced by the K component of the angular momentum; the angular distribution for any given mass bin is therefore forward-backward symmetric. Since fission is a binary process, this symmetry also implies that the mean mass of the fission products does not depend on the center of mass angle. Quasifission processes bypass the compound nucleus stage and can occur in time scales shorter than the rotation period of the system. This can lead to a broken forward-backward symmetry of the angular distribution for a particular fission fragment mass, or conversely, to an angular dependence of the mean fragment mass. A broken fragment mass symmetry is not always observed in quasifission reactions. If the time scale for quasifission equals several rotational periods of the projectile-target system, this signature will be washed out. As an absolute, model independent, upper bound on the complete fusion cross section we therefore include only that fraction of the cross section that obeys this symmetry. This is shown as open circles in Fig. 11. However, more stringent limitations arise from the requirement of the angular distributions and mass widths expected for compound fission as discussed below.

2. Angular anisotropies

In the quasifission process the compact saddle point is not reached, and the K distribution may correspond to a statisti-

cal equilibrium at shapes more elongated than the true saddle point or it may not be equilibrated at all. A K distribution which is narrower than predicted by the saddle point model results in larger anisotropies of the fissionlike fragments [2]. Following the method of Ref. [3], we have estimated the maximum compound fission cross section by assuming a sharp division in angular momentum space, at $I_{\mathrm{C.F.}}$, between compound fission and quasifission, and fitting the angular distribution by varying the value of $I_{\mathrm{C.F.}}$. The assumption for the parameter, $\mathscr{J}_o/\mathscr{J}_{\mathrm{eff}}$, controlling the angular distributions for both components are identical to those of Ref. [3]. For the $^{32}\mathrm{S}+^{182}\mathrm{W}$ system the full angular distribution (integrated over all fission fragment masses) was used whereas only the $A=107$ mass bin was used for $^{48}\mathrm{Ti}+^{166}\mathrm{Er}$ and $^{60}\mathrm{Ni}+^{154}\mathrm{Sm}$. The resulting estimate of the maximum complete fusion-fission cross sections for $^{32}\mathrm{S}+^{182}\mathrm{W}$ are listed in Table II. For the $^{48}\mathrm{Ti}+^{166}\mathrm{Er}$ system only the data for bombarding energy of $E_{\mathrm{lab}}=270$ MeV was of sufficient quality to perform this analysis, which resulted in an upper complete fusion fraction of $\sigma_{\mathrm{C.F.}}/\sigma_{\mathrm{fis}}=44\%$. This fraction was used at the other beam energies measured for this system. The maximum complete fusion fractions for symmetric fission in the $^{60}\mathrm{Ni}+^{154}\mathrm{Sm}$ system were $\sigma_{\mathrm{C.F.}}/\sigma_{\mathrm{fis}}=42$, 32, and 45% for beam energies of 339, 390, and 421 MeV, respectively. These estimates are clearly model dependent. The sharp division between complete fusion and quasifission in angular momentum space is an oversimplification and the value of the parameter, $\mathscr{J}_o/\mathscr{J}_{\mathrm{eff}}=1.5$ for all quasifission events is somewhat arbitrary and does not reflect the dependence on the various parameters controlling the reaction dynamics. However, despite the crude assumptions underlying this analysis we believe that it reflects the salient features of the reaction and we assign an error of about $\pm 25\%$ to this estimate of the upper limit of the complete fusion cross section.

3. Width of mass distributions

For compound nucleus fission, we expect that the width of the fragment mass distribution will be a smooth function of the temperature at the scission point and that it is independent of the entrance channel (except for possible angular momentum effects). In quasifission reactions, however, the projectile-target system separates before the mass asymmetry degree of freedom is fully equilibrated, and deviations may therefore be expected. In the case of the asymmetric channels that were used to reach ^{214}Th, a possible signature for quasifission would be an increasing variance of the mass distribution. The estimate of the maximum compound fission cross section is therefore obtained from Gaussian mass distributions with a standard deviation given by Eq. (7) (solid curve in Fig. 12) and normalized to the complete fusion fraction for the symmetric mass obtained from the analysis of the angular distribution. The corresponding mass distributions are shown as solid curves in Fig. 11.

The final estimates of the upper limit for the complete fusion cross section are listed in Table II and shown as filled triangles in Fig. 10, where they are compared with the prediction of the extra push model (long-dashed curves) using the parameters of Ref. [5]. The dotted curves represents the contribution to σ_{touch} from partial waves for which the fission barrier is positive, $\sigma_{B_f>0}$. We find that the upper limits for complete fusion found in this analysis are much lower than the limits set by the $B_f>0$ criterion indicating that the restrictions set by the extra push model are effective for most of the data, except the highest energy point for each system. It is evident that the overall trend of $\sigma_{\mathrm{C.F.,max}}$ is in good agreement with the expectation based on the extra push model.

However, comparing $\sigma_{\mathrm{C.F.,max}}$ to the short-dashed curves in Fig. 10, which reflects the condition $B_f>T$ (T is the temperature of the compound nucleus) as suggested by Gavron *et al.* [21], we see that most of the data satisfies this criterion for complete fusion keeping in mind that the experimental points are upper limits. It is, however, not entirely clear how stringent this more restrictive criterion is. Thus recent studies [22] have shown that the fission process can be strongly retarded at high excitation energies due to the dynamics of the process. This allows neutron emission to compete favorably against fission and may allow the system to cool sufficiently to relax this limit substantially before fission takes place. The present data therefore appear to show dynamical restrictions for complete fusion over and above those dictated by the stability of the fused system.

V. SUMMARY AND CONCLUSIONS

Full angular distributions for elastic/quasielastic, deep-inelastic scattering and fissionlike processes have been measured for three projectile-target combinations leading to ^{214}Th in complete fusion. A complete accounting for the reaction cross section was carried out by comparing the sum of the individual components (deep inelastic plus fissionlike reactions) to the total cross section for damped reactions derived from the angular distributions for elastic/quasielastic scattering. Evidence for quasifission was observed by comparing the angular anisotropy with predictions of the saddle point model for the $^{32}\mathrm{S}+^{182}\mathrm{W}$ system.

Upper limits for complete fusion fission were determined by requiring that this component of the cross section (1) exhibit forward-backward angular symmetry for all mass divisions, and show (2) angular anisotropies, and (3) fragment mass widths, of a magnitude expected for compound nucleus decay. This analysis reveals that only a small fraction of the reaction cross section is associated with complete fusion for the $^{48}\mathrm{Ti}+^{166}\mathrm{Er}$ and $^{60}\mathrm{Ni}+^{154}\mathrm{Sm}$ systems, the remainder being attributed to quasifission processes.

The cross section data show good agreement with the predictions of the extra push model, and, in particular, the observed upper limits on the complete fusion component appear to be suppressed by the reaction dynamics contained in this model over and above the requirements of relative stability of the compound system in terms of a nonvanishing fission barrier.

ACKNOWLEDGMENTS

This work was carried out under the auspices of the U.S. Department of Energy under Contract No. W-31-109-Eng-38.

[1] B. B. Back, H.-G. Clerc, R. R. Betts, B. G. Glagola, and B. D. Wilkins, Phys. Rev. Lett. **46**, 1068 (1981).
[2] B. B. Back, R. R. Betts, K. Cassidy, B. G. Glagola, J. E. Gindler, L. E. Glendenin, and B. D. Wilkins, Phys. Rev. Lett. **50**, 818 (1983).
[3] B. B. Back, Phys. Rev. C **31**, 2104 (1985).
[4] J. Tōke, R. Bock, G. X. Dai, A. Gobbi, S. Gralla, K. D. Hildenbrand, J. Kuzminski, W. F. J. Müller, A. Olmi, H. Stelzer, B. B. Back, and S. Bjørnholm, Nucl. Phys. **A440**, 327 (1985); J. Tōke, R. Bock, G. X. Dai, A. Gobbi, S. Gralla, K. D. Hildenbrand, J. Kuzminski, W. F. J. Müller, A. Olmi, W. Reisdorf, S. Bjørnholm, and B. B. Back, Phys. Lett. **142B**, 258 (1984).
[5] W. Q. Shen, J. Albinski, R. Bock, G. X. Dai, A. Gobbi, S. Gralla, K. D. Hildenbrand, N. Herrmann, J. Kuzminski, W. F. J. Müller, H. Stelzer, J. Tōke, B. B. Back, S. Bjørnholm, S. P. Sørensen, A. Olmi, and G. Guarino, Europhys. Lett. **1**, 113 (1986).
[6] W. Q. Shen, J. Albinski, A. Gobbi, S. Gralla, K. D. Hildenbrand, N. Herrmann, J. Kuzminski, W. F. J. Müller, H. Stelzer, J. Tōke, B. B. Back, S. Bjørnholm, and S. P. Sørensen, Phys. Rev. C **36**, 115 (1987).
[7] C. Lebrun, F. Hanappe, J. F. Lecolley, F. Lefebvres, C. Ngô, J. Péter, and B. Tamain, Nucl. Phys. **A321**, 207 (1979).
[8] W. J. Swiatecki, Phys. Scr. **24**, 113 (1981).
[9] S. Bjørnholm and W. J. Swiatecki, Nucl. Phys. **A391**, 471 (1982).
[10] J. G. Keller, B. B. Back, B. G. Glagola, D. Henderson, S. B. Kaufman, S. J. Sanders, R. H. Siemssen, F. Videbaek, B. D. Wilkins, and A. Worsham, Phys. Rev. C **36**, 1364 (1987).
[11] V. E. Viola, Jr., B. B. Back, K. L. Wolf, T. C. Awes, C. K. Gelbke, and H. Breuer, Phys. Rev. C **26**, 178 (1982).
[12] W. Bohne, W. Galster, K. Grabisch, and H. Morgenstern, Nucl. Instrum. Methods A **240**, 145 (1985).
[13] M. Ogihara, Y. Nagashima, W. Galster, and T. Mikumo, Nucl. Instrum. Methods A **251**, 313 (1986).
[14] V. E. Viola, Jr., Nucl. Data Sect. A **1**, 391 (1966); V. E. Viola, K. Kwiatkowski, and M. Walker, Phys. Rev. C **31**, 1550 (1985).
[15] H. Oeschler, H. L. Harvey, D. L. Hillis, and K. S. Sim, Nucl. Phys. **A325**, 463 (1979).
[16] I. Halpern and V. M. Strutinski, *Proceedings of the Second UN International Conference on the Peaceful Uses of Atomic Energy, Geneva, Switzerland, 1957* (United Nations, Geneva, Switzerland, 1958), p. 408.
[17] B. G. Glagola *et al.*, Bull. Am. Phys. Soc. **26**, 550 (1981).
[18] A. J. Sierk, Phys. Rev. C **33**, 2039 (1986).
[19] The scission point model for describing angular distributions was originally suggested by T. Ericson and V. Strutinski, Nucl. Phys. **8**, 284 (1958); **9**, 689 (1959), and has more recently been studied by P. Bond, Phys. Rev. Lett. **52**, 414 (1984), and H. H. Rosner, J. R. Huizenga, and W. U. Schröder, *ibid.* **53**, 38 (1984); the curve shown is based on a scission point shape which reflects the known total kinetic energy in fission; see Ref. [3].
[20] M. G. Itkis, S. M. Luk'yanov, V. N. Okolovich, Yu. É. Penionzhkevich, A. Ya. Rusanov, V. S. Salamatin, G. N. Smirenkin, and G. G. Chubaryan, Yad. Fiz. **52**, 23 (1990) [Sov. J. Nucl. Phys. **52**, 15 (1990)].
[21] A. Gavron, P. Eskola, A. J. Sierk, J. Boissevain, H. C. Britt, K. Eskola, M. M. Fowler, H. Ohm, J. B. Wilhelmy, S.Wald, and R. L. Ferguson, Phys. Rev. Lett. **52**, 589 (1984).
[22] P. Paul and M. Thoennessen, Annu. Rev. Nucl. Part. Sci. **44**, 65 (1994).